metals

Article

Microstructure and Mechanical Properties of Biomedical Ti-Zr-Nb-Ta-Sn High-Entropy Alloys

Maxim Ozerov [1,*], Nikita Yurchenko [1,2], Vitaly Sokolovsky [1], Elena Nozdracheva [1], Evgeniya Panina [1], Sergey Nadezhdin [1], Nikita Stepanov [1,2] and Sergey Zherebtsov [1,2]

[1] Laboratory of Bulk Nanostructured Materials, Belgorod State University, 308015 Belgorod, Russia
[2] World-Class Research Center "Advanced Digital Technologies", State Marine Technical University, 198095 Saint Petersburg, Russia
* Correspondence: ozerov@bsu.edu.ru; Tel.: +7-4722-58-54-16

Abstract: Ti(50-x)Zr38NbxTa8Sn4 high-entropy alloys with x = 0, 10, and 20 at.% were produced by vacuum arc melting in a high-purity argon atmosphere. The initial microstructures consisted of equiaxial bcc grains with sizes of 115 ± 30 μm, 250 ± 60 μm, and 280 ± 70 μm for the Ti30Nb20, Ti40Nb10, and Ti50Nb0 alloys, respectively. The Ti30Nb20 and Ti40Nb10 alloys showed untypical mechanical behavior with a short strain-hardening stage followed by a gradual decrease in flow stress after reaching the yield point. Although these two alloys had some inclination toward macroscopic strain localization, their tensile elongation was similar to that obtained in the Ti50Nb0 alloy, which had a more extended stage of uniform deformation. The differences were associated with distinct microstructures observed after deformation to fracture. The formation of dislocation bands and the activation of cross-slip at the microscale, as well as the appearance of kink bands at the mesoscale, can result in plastic instability. In contrast, a lamellar-like microstructure with parallel dislocation bands, such as the one observed in the Ti50Nb0 alloy, can ensure a more stable mechanical behavior. The developed alloys (Ti30Nb20 and Ti40Nb10) have properties that make them highly attractive for biomedical application due to a combination of very high yield strengths (1090 and 930 MPa, respectively), low Young's moduli (~78 and ~69 GPa, respectively), reasonable ductility, and excellent biocompatibility.

Keywords: high-entropy alloys; microstructure; EBSD analysis; mechanical properties; biomedical application

check for updates

Citation: Ozerov, M.; Yurchenko, N.; Sokolovsky, V.; Nozdracheva, E.; Panina, E.; Nadezhdin, S.; Stepanov, N.; Zherebtsov, S. Microstructure and Mechanical Properties of Biomedical Ti-Zr-Nb-Ta-Sn High-Entropy Alloys. *Metals* **2023**, *13*, 353. https://doi.org/10.3390/met13020353

Academic Editor: Jiro Kitagawa

Received: 28 December 2022
Revised: 31 January 2023
Accepted: 4 February 2023
Published: 10 February 2023

Copyright: © 2023 by the authors. Licensee MDPI, Basel, Switzerland. This article is an open access article distributed under the terms and conditions of the Creative Commons Attribution (CC BY) license (https://creativecommons.org/licenses/by/4.0/).

1. Introduction

Materials used for the production of biomedical implants replacing bone tissue should possess a number of mechanical and functional properties, including low elastic modulus to prevent bone resorption due to the stress shielding effect [1], high yield strength, high fatigue strength, and good ductility that would allow them to withstand the loads of physical activity. Biomedical materials should also meet the obvious strict requirements for biocompatibility, have high wear resistance (and a low coefficient of friction in some cases), and be corrosion-resistant in contact with tissue or body fluids [2,3]. The Ti6Al4V alloy is one of the most commonly used metallic materials in biomedicine [4]. However, the presence of some cytotoxic elements (Al and V) requires the modification of its chemical composition by using elements that are harmless for the human body. One of the promising solutions is related to the development of new biomedical high-entropy alloys (HEAs) comprising biocompatible elements (Ti, Nb, Zr, Sn, etc.). HEAs are usually defined as multicomponent alloys consisting of several (usually, at least five) basic elements, taken in approximately equal proportions (5–35 at.%) [5]. This approach can result in the production of new compositions with significantly improved mechanical and tribological properties, while maintaining excellent biocompatibility [6]. Although the application of HEAs in

biomedicine is very promising [7–11], the complex mechanical and functional properties (high strength and ductility, low modulus of elasticity, good corrosion and wear resistance) of these alloys should be carefully examined on a case-by-case basis. Therefore, a comprehensive, systematic analysis of the structure–properties relationships of these alloys is needed.

It should be noted that the development of new HEAs with a high percentage of Ti has intensified in recent times. In [12], a new TiZrHfNbTa alloy comprising only non-toxic and hypoallergenic elements was studied by Yuan et al. This HEA showed a good combination of low elastic modulus (57 GPa, nearly half of that of traditional biomedical titanium alloys such as Ti6Al4V), advanced mechanical properties, biocompatibility, and low magnetic susceptibility. Gurel et al. [13] studied the compositions of TiTaHfNb, TiTaHfNbZr, and TiTaHfMoZr. All three bcc alloys also exhibited lower Young's modulus in comparison with conventional biomedical materials that can be used for the production of implants. The high-entropy TiTaHfNb alloy had the highest energy-absorbing capacity and the highest ductility of the three systems. The non-equiatomic HEAs of the Ti-Ta-Hf-Nb-Zr system were also studied by Yang et al. [14]. For example, Ti1.5Ta0.5Hf0.5Nb0.5Zr showed extremely high pitting corrosion resistance. The elastic modulus and hardness of Ti1.5Ta0.5Hf0.5Nb0.5Zr were 98.57 GPa and 3.02 GPa, respectively. The wear resistance was found to be better than that of 316 L, CoCrMo, and Ti6Al4V. With excellent wear resistance, similar wettability, lower Young's modulus, and significantly better corrosion resistance, the configuration of this high-entropy alloy system (Ti1.5Ta0.5Hf0.5Nb0.5Zr) has shown promising potential in the biomedical field, warranting further study of the biocompatibility and cytotoxicity of this composition.

Given the incredibly vast compositional space of HEAs, it is necessary to select appropriate alloying elements in order to exploit the required properties with regard to designing new alloys. In this study, three new HEAs with high contents of titanium and zirconium and chemical compositions Ti30Zr38Nb20Ta8Sn4, Ti40Zr38Nb10Ta8Sn4, and Ti50Zr38Ta8Sn4 were introduced. Their structure and properties were examined with particular attention to the effect of chemical composition on mechanical behavior. The addition of Nb and/or Ta resulted in the formation of a bcc phase with lower Young's modulus in comparison with the hcp phase (intrinsic for Ti alloys with a low percentage of β-stabilizing elements). Sn (as well as Zr) is often used in titanium alloys to improve strength without noticeable changes in ductility.

2. Materials and Methods

Laboratory-size specimens (~60 g) of the Ti30Zr38Nb20Ta8Sn4, Ti40Zr38Nb10Ta8Sn4, and Ti50Zr38Ta8Sn4 alloys (hereafter designated as Ti30Nb20, Ti40Nb10, and Ti50Nb0, respectively) were produced by vacuum arc melting using Ti, Zr, Nb, Ta, and Sn granules (≥99.9 wt.% purity in each case) in a high-purity argon atmosphere. Before the melting procedure, the chamber was degassed and flushed with argon 3 times; the last vacuuming reached 10^{-5}–10^{-6} millibars. The microstructure of the obtained alloys was analyzed using scanning electron microscopy (SEM) with electron backscatter diffraction (EBSD) analysis. Specimens for EBSD observations were prepared through careful mechanical polishing. EBSD was conducted with a FEI Quanta 600 FEG (Thermo Fisher Scientific, Hillsboro, OR, USA) field-emission-gun scanning electron microscope (FEG-SEM) operated at an accelerating voltage of 20 kV and equipped with a TSL OIM™ system (EDAX, Pleasanton, CA, USA). The maps were obtained using a scan step size of 0.05 μm. The size of each scanned region was 1 × 1 mm^2. The grain size was estimated using at least 3 images covering ~150 grains. Kernel average misorientation (KAM) maps were used for a more comprehensive analysis of the microstructures. KAM is the average misorientation angle of a given pixel in an EBSD map with respect to its neighbors. Therefore, it shows the local orientation spread and can be used as a measure of excess dislocation density of the same sign and local lattice distortion/curvature.

Tensile tests were conducted using an Instron 5882 machine (Instron, Canton, USA) at room temperature with an initial strain rate of 10^{-3} s^{-1}. Dog-bone-shaped tensile specimens with a gauge of 6 × 3 × 1.5 mm^3 were used. The digital image correlation (DIC) technique was employed to visualize the distribution of local strains produced during the tensile tests. The in-plane Lagrangian strains were measured using a commercial Vic-3D™ system (Correlated Solutions, Inc., Irmo, SC, USA). The resonance frequency damping analysis (RFDA) method [15] using the IMCE measuring system (IMCE NV, Genk, Belgium) was applied for Young's modulus determination. The size of the measured samples was 55 × 12 × 5 mm^3. Microhardness was measured using an automated Vickers hardness testing machine (Instron, Norwood, MA, USA) with a 300 g load for 50 s.

A direct-contact cytotoxicity assay of the composites was carried out in vitro using rat mesenchymal stem cells (MSCs). A photometry technique using a microplate photometer Multiskan FC and an MTT reagent (cat. M5655, Sigma-Aldrich, St. Louis, MO, USA) [16] was utilized. MSCs with metal samples were cultivated in a CO_2 incubator (95% humidity, 37 °C temperature, 5% CO_2) for 72 hours in a nutrient medium (DMEM/F12) (cat. 11320033 Thermo Scientific, Waltham, MA, USA) supplemented with 10% fetal bovine serum (Cytiva, HyClone, USA) and antibiotics. A polystyrene surface without a composite disc was used as a control sample. Cell viability was calculated using the formula Cell viability (%) = (A) test/(A) control × 100, where (A) test is the absorption of the test sample, and (A) control is the control sample absorption. The obtained results were statistically processed using the Wilcoxon T-test on the Statistica 6.0 software (StatSoft, Krakow, Poland). A qualitative assessment of cytotoxicity was performed microscopically using an inverted optical microscope Eclipse Ti-S (Nikon, Tokyo, Japan) equipped with a digital camera.

3. Results and Discussion

3.1. Initial Microstructure

In the initial conditions, the microstructure of all three alloys consisted of bcc equiaxed grains (Figure 1). According to the EBSD analysis, an increase in the Ti/Nb ratio resulted in grain coarsening. The grain sizes were estimated to be 115 ± 30 μm, 250 ± 60 μm, and 280 ± 70 μm for the Ti30Nb20, Ti40Nb10, and Ti50Nb0 alloys, respectively. One of the most plausible explanations can be related to a decrease in the diffusion rate and an increase in the percentage of more refractory Nb. Similar effects of Nb on grain size have been previously reported in [17].

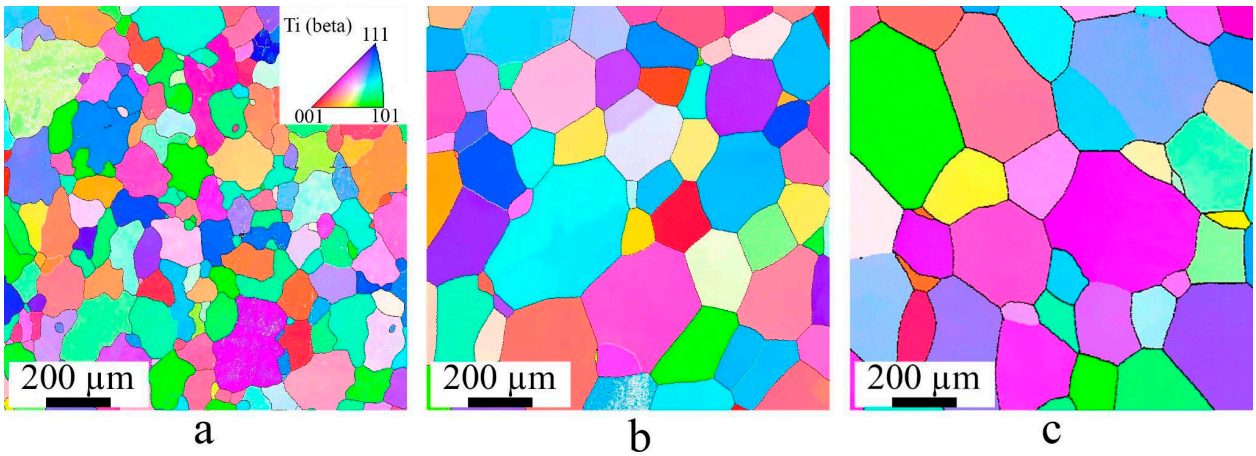
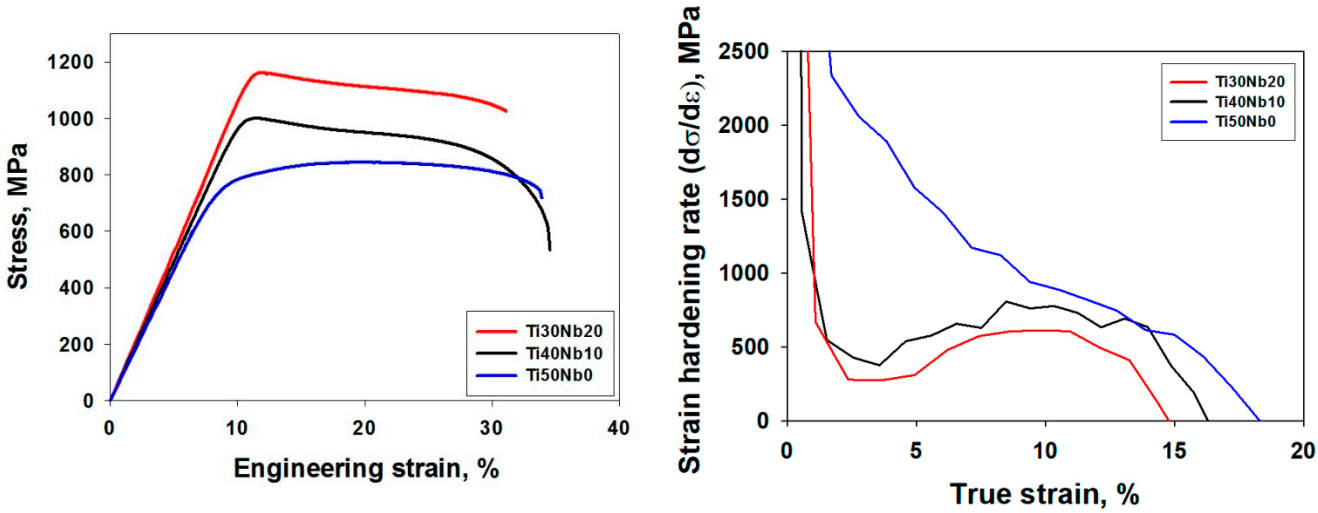


Figure 1. IPF maps of the initial microstructure of Ti30Nb20 (**a**), Ti40Nb10 (**b**), and Ti50Nb0 (**c**) alloys.

3.2. Mechanical Properties

Engineering stress-strain tensile curves of the alloys obtained at room temperature are shown in Figure 2a; the data on the mechanical properties are collected in Table 1. The Ti30Nb20 and Ti40Nb10 alloys demonstrated much higher (>900 MPa) values of yield

strength compared to their Ti50Nb0 counterpart (Figure 2a, Table 1). However, unlike the Ti50Nb0 alloy, which had typical post-yielding behavior with relatively large (~15%) uniform elongation, the Ti30Nb20 and Ti40Nb10 alloys, after reaching the yield point, showed a short strain-hardening stage followed by a gradual decrease in flow stress. Nevertheless, the Ti30Nb20 and Ti40Nb10 alloys also achieved high total elongations ($\delta > 20\%$). The analysis of the strain-hardening rate curves revealed that the Ti50Nb0 alloy had a "normal" decay of $d\sigma/d\varepsilon$ with strain (Figure 2b). However, the Ti30Nb20 and Ti40Nb10 alloys showed "dropped-then-recovered" $d\sigma/d\varepsilon$ curves (the curve of the Ti30Nb20 alloy was slightly shifted to a greater strain compared to that of its Ti40Nb10 counterpart), which could be attributed to the dynamic Hall–Petch effect (see Section 4) [18,19].



(**a**) (**b**)

Figure 2. Engineering stress-strain curves of the program alloys obtained during tension at 20 °C with a nominal strain rate of 10^{-3} s^{-1} (**a**) and corresponding strain-hardening rate behavior as a function of true strain (**b**).

Table 1. Mechanical properties and density of all the program alloys.

Alloy	Young's Modulus, GPa	Yield Strength, MPa	δ,%	Microhardness, HV	Density, g/cm^3
Ti30Nb20	77.7 ± 0.1	1090 ± 50	24 ± 2	321 ± 5	7.24 ± 0.04
Ti40Nb10	68.8 ± 0.1	930 ± 45	29 ± 3	280 ± 6	6.26 ± 0.04
Ti50Nb0	57.5 ± 0.1	690 ± 40	25 ± 2	244 ± 5	5.99 ± 0.04

The DIC analysis (Figure 3) showed somewhat different strain localizations in the alloy specimens during tension. The Ti30Nb20 and Ti40Nb10 alloys showed a less homogeneous strain distribution compared to the Ti50Nb0 alloy starting from the early stage of deformation (H5%) (Figure 3a–c). Localization became more obvious at the strain corresponding to the end of the uniform deformation (H15%) stage in the Ti50Nb0 alloy (Figure 3d–f), and this difference between the three alloys remained until the fracture of the specimens (Figure 3g–i).

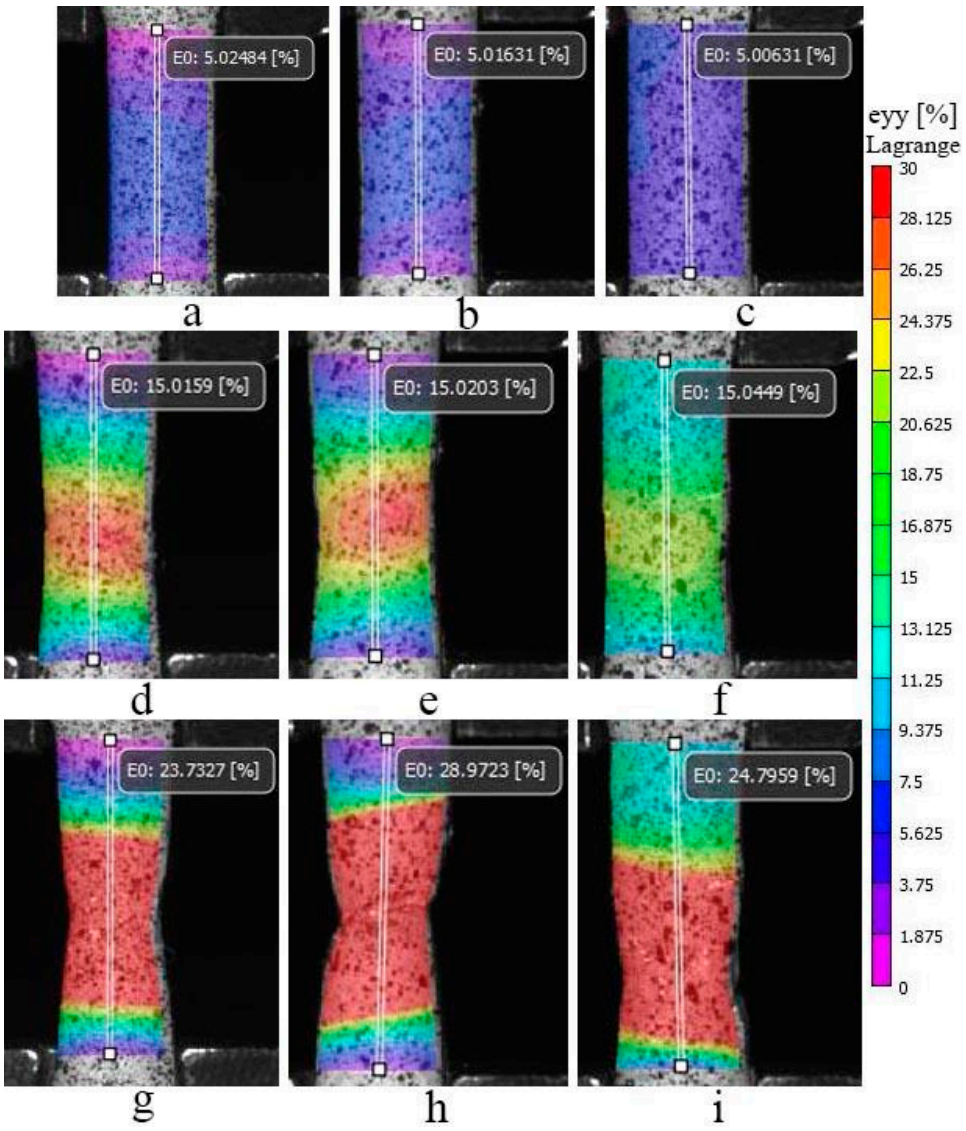


Figure 3. DIC images of tensile specimens of Ti30Nb20 (**a**,**d**,**g**), Ti40Nb10 (**b**,**e**,**h**), and Ti50Nb0 (**c**,**f**,**i**) alloys showing the strain distribution along the gauge.

The microhardness of the alloys corresponded to the yield strength. The strongest alloy, Ti30Nb20, showed the highest value with 321HV, while Ti50Nb0, with the lowest yield strength, showed a value of hardness of 244 HV (Table 1). Young's modulus values were also related to strength: E = 77.7 GPa was found for the Ti30Nb20 alloy, while Ti50Nb0 showed a Young's modulus of 57.5 GPa (Table 1). The Young's modulus values obtained for all three alloys are comparable to those of human bone and, therefore, can be considered suitable for biomedical application [20].

3.3. Deformed Microstructure

In order to gain insights into the microstructure evolution during tensile deformation, we performed an EBSD analysis on the fractured specimens near the fracture surfaces (Figure 4). The deformation of the Ti30Nb10 alloy (Figure 4a) did not result in pronounced changes to the microstructure; the variation in misorientation within grains was relatively low. However, black dots (with CI < 0.1) near grain boundaries suggested high residual stresses, due to which a reliable determination was not possible. Additionally, kink bands (KBs) (usually lens-shaped) were observed in the microstructure. The thickness of the kinks varied from ~15 to ~30 μm. The misorientation angle of the KB boundaries was close to

40–50°. The kernel average misorientation maps (KAM) showed notable strain localization along the boundaries of grains and, particularly, of KBs, while the grain interiors remained lowly deformed (Figure 4b).

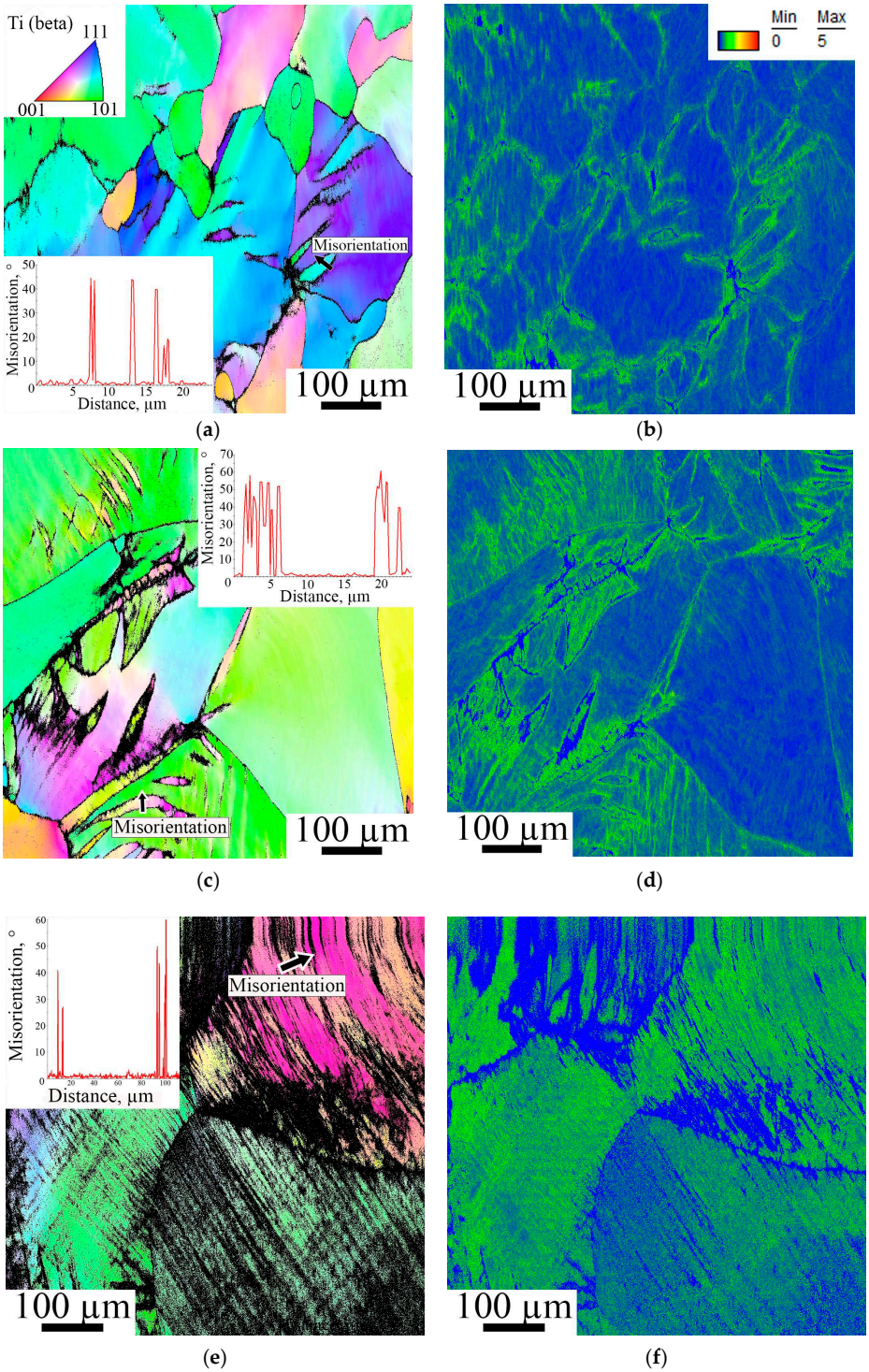


Figure 4. EBSD maps of deformed microstructures near the fracture surfaces of specimens after tensile tests; (**a**,**b**)—Ti30Nb20, (**c**,**d**)—Ti40Nb10, (**e**,**f**)—Ti50Nb0; (**a**,**c**,**e**)—IPF maps, (**b**,**d**,**f**)—kernel average misorientation maps. Tension direction is horizontal in all cases; the fracture surfaces are located near the left side of the images.

A similar microstructure with numerous KBs was observed in specimens of the Ti40Nb10 alloy after fracture (Figure 4c). However, an increase in the Ti/Nb ratio re-

sulted in the formation of a lamellar-like substructure in some grains. The KAM map also confirmed a more uniform deformation in the Ti40Nb10 alloy (compared to that of its Ti30Nb10 counterpart), which suggested an increase in dislocation density within grains, although some grains were still not involved in plastic deformation (Figure 4d).

The complete substitution of Nb with Ti in the Ti50Nb0 alloy changed the character of the microstructure's response to plastic strain noticeably. Unlike the Ti30Nb20 and Ti40Nb10 alloys, deformation of the Ti50Nb0 alloy resulted in the formation of a well-developed lamellar substructure (Figure 4e). The thickness of the lamellae was 1–5 µm. The misorientation across the lamellae was almost constant, suggesting dislocation activity rather than twinning. KBs were rarely observed in the microstructure of Ti50Nb0 after deformation. The KAM map also indicated a relatively uniform distribution of dislocations in the microstructure (Figure 4e).

An additional TEM analysis confirmed a single-phase bcc structure in all three alloys (inserts in Figure 5a–c) and revealed some differences in the character of dislocation slip among the alloys. In the Ti50Nb0 alloy, dislocations tended to localize in parallel dislocation bands (DBs, Figure 5c) forming the lamellar-like microstructure observed in the EBSD maps (Figure 4e). Meanwhile, in the Ti30Nb20 and Ti40Nb10 alloys, DBs were found to be mutually intersected due to the development of cross-slip (Figure 5a,b). Between parallel or intersected DBs, the dislocation density was found to be noticeably reduced.

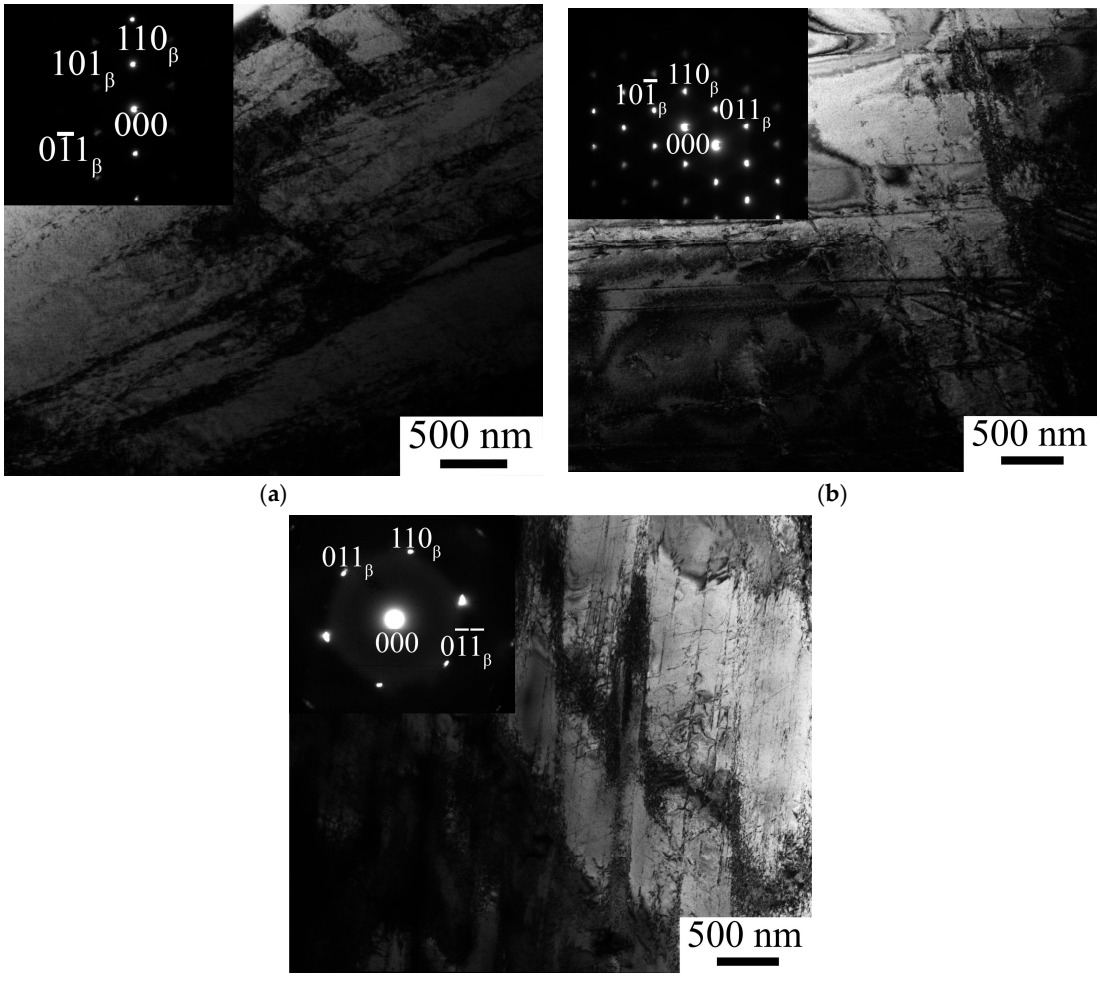


Figure 5. TEM images of deformed microstructures near the fracture surfaces of specimens after tensile tests: (**a**)—Ti30Nb20, (**b**)—Ti40Nb10, (**c**)—Ti50Nb0.

3.4. Cytotoxicity

The viability of mesenchymal stem cells (MSCs) during cultivation with the alloy samples was quantified as follows: 78.30%, 83.49%, and 99.53% for the Ti30Nb20, Ti40Nb10, and Ti50Nb0 alloys, respectively. These results were in agreement with the quantitative assessment of cytotoxicity (Figure 6). In the control group (Figure 6a), MSCs showed a typical morphology and were represented by spindle-shaped fibroblast-like cells that densely covered the bottom surface of a 96-well culture plate. For the Ti30Nb20 alloy, the MSC layer was not uniform and somewhat sparse, and it was in weak contact with the sample and apoptotic cells (Figure 6b). In contrast, the Ti40Nb10 and Ti50Nb0 alloys did not cause noticeable changes in the morphology of the MSCs in comparison to the control group, i.e., the cells formed a dense layer even when in contact with the alloy samples (Figure 6c,d).

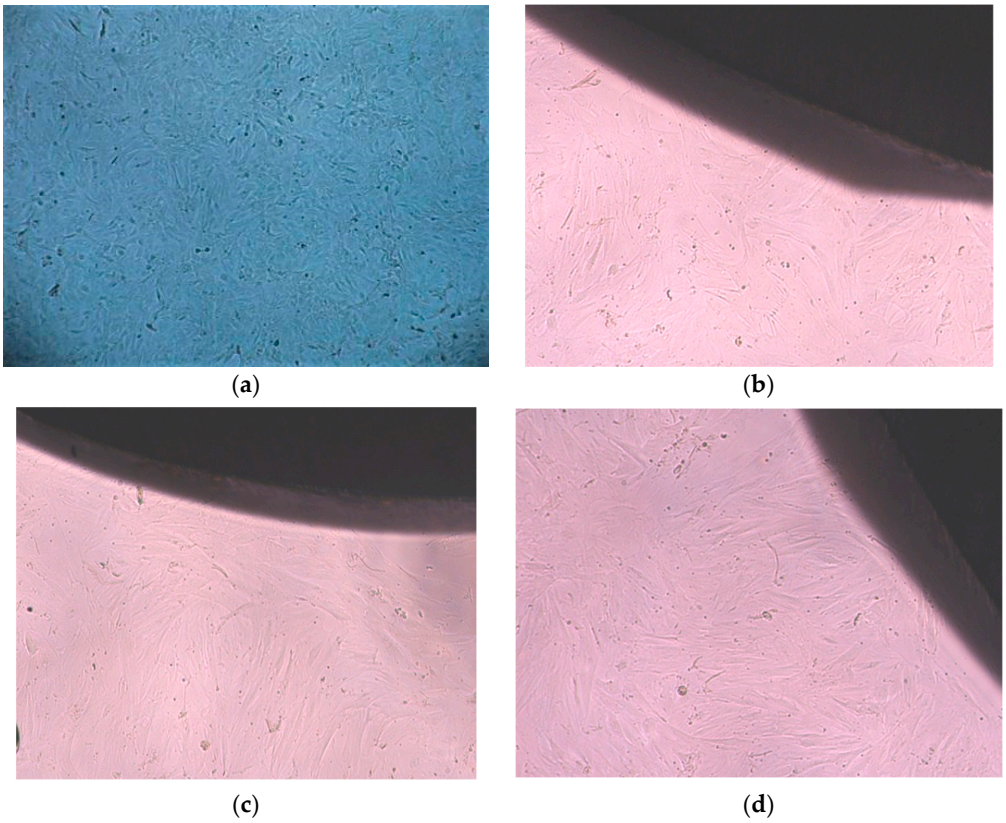


Figure 6. Morphology of MSCs in the control sample (without metallic specimen) (**a**) and Ti30Nb20 (**b**), Ti40Nb10 (**c**), and Ti50Nb0 (**d**) alloys. Magnification was ×100.

4. Discussion

The obtained results suggest significant differences in the properties and mechanical behavior of the Ti(50-x)Zr38NbxTa8Sn4 alloys depending on the content of Ti and Nb. The most apparent change is related to the decrease in strength and Young's modulus as the Ti content increases (Table 1). The mechanical properties of HEAs are known to be dependent on the choice and concentration of the constitutive elements (the so-called "cocktail effect" [21], which can be noteworthy). For instance, the present study revealed a linear relationship between the Nb content and Young's modulus in the program alloys (Figure 7). The vast knowledge obtained from bcc Ti alloys suggests that Nb doping generally decreases the modulus of the materials [22–25], yet this effect strongly depends on the Nb concentration. However, at a certain concentration range, the opposite trend (i.e., an increase in the moduli) can be observed [26]. The same trend seems to hold true for the program alloys.

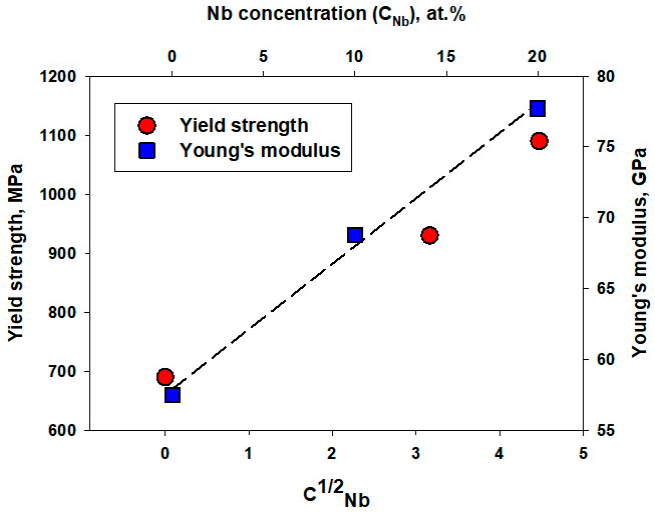


Figure 7. Dependence of the Young's modulus of the program alloys on Nb percentage (C_{Nb}) and yield strength on $C^{1/2}_{Nb}$.

In terms of strength, Nb atoms can generate lattice elastic strains due to differences in atomic size and modulus compared to the atoms of the other constitutive elements. The resulting increase in strength (i.e., solid solution strengthening), in this case, is expected to be proportional to $C^{1/2}_{Nb}$ according to the classic Fleisher approach [27]. The comparison between experimental yield strength values and $C^{1/2}_{Nb}$ (Figure 7) suggests that solid solution strengthening is the main responsible for strength variations in the program alloys. Other sources, such as grain boundary strengthening [28,29], are likely to have a minor effect.

Another interesting aspect found in this study is the difference in mechanical behavior of the studied alloys after yielding. The Ti30Nb20 and Ti40Nb10 alloys showed a gradual decrease in flow stress in the post-yielding region, which was due to strain localization without early necking (Figure 3). In contrast, the Ti50Nb0 alloy demonstrated more uniform deformation after the yield point, as reported previously for a number of alloys [30–33]. The tendency toward apparent premature strain localization can be attributed to a non-uniform spatial distribution of dislocations in the microstructure. For example, the Al-induced B2 ordering of a NbTiZr HEA resulted in the localization of plastic deformation in multiple DBs [34]. Instead of deteriorating the mechanical properties, this localization increased the ductility of Al-containing alloys compared to the Al-free NbTiZr HEA, in which dislocation distribution was uniform.

In the Ti30Nb20 and Ti40Nb10 alloys, the formation of DBs and the activation of cross-slip were also observed (Figure 5a,b). In addition to microscopic localization, noticeable heterogeneity in strain distribution at the mesoscale (Figure 4b,d) resulted in macroscopic plastic flow instability (Figure 3). Moreover, the formation of KBs (Figure 4), which caused geometric softening due to stress relaxation and crystal reorientation [35], seemed to be another factor contributing to a reduction in flow stress. The KAM maps showed a considerable increase in dislocation density around KBs, indicating the KB boundaries could contribute to strengthening, as seen in the upturn trend in the $d\sigma/d\varepsilon$ curves of the Ti30Nb20 and Ti40Nb10 alloys (the so-called dynamic Hall–Petch effect) (Figures 2b and 4). In contrast, the lamellar-like KB-free microstructure with parallel DBs (without visible cross-slipping; Figure 5c) prevented early macroscopic localization in the Ti50Nb0 alloy, resulting in relatively larger uniform elongation (Figures 2a and 3).

The observed difference can probably be attributed to the stability of the bcc phase in these alloys. In Ti alloys, the stability of the bcc phase is typically evaluated using the molybdenum equivalent, in which the contribution of all bcc-stabilizing elements is calculated using the equation [36] $Mo_{eq.}$ = 1.0 Mo + 0.67 V + 0.44 W + 0.28 Nb + 0.22 Ta + 2.9 Fe + 1.6 Cr − 1.0 Al. In our case, the program alloys have $Mo_{eq.}$ = 7.36, 4.56, and

1.76 for Ti30Nb20, Ti40Nb10, and Ti50Nb0, respectively. This approach, without a doubt, cannot be used for HEAs with a high content of Ti, since, according to the accepted classification, a $Mo_{eq.} < 3$ is typical for near α alloys with an hcp lattice, while Ti50Nb0 has the bcc structure.

Another approach for predicting the main deformation mechanism in Ti alloys was proposed by Morinaga and co-authors [37]. In this approach, the bond order Bo and the metal d-orbital energy level Md were used to predict the β-phase stability in titanium alloys. Later, the Bo–Md map was used to tailor the chemical composition of Ti-rich HEAs [38]. Although some Ti-rich HEAs can indeed be clustered as per their main deformation mechanism (Figure 8), the Ms = RT is barely a straight line as it was initially proposed by Lilensten and co-authors [37]. Indeed, the results obtained in the present work show that the program alloys are located above (Ti30Nb20), on (Ti40Nb10), and below (Ti50Nb0) the Ms = RT line, but none of them exhibits TRIP/TWIP effects, and the two upper alloys (Ti30Nb20 and Ti40Nb10) have similar behavior, which differs considerably from that of the Ti50Nb0 alloy. Furthermore, another well-known HfNbTaTiZr HEA with a microstructure evolution essentially similar to that of Ti30Nb20 and Ti40Nb10 is located well above the proposed Ms = RT line (Figure 8).

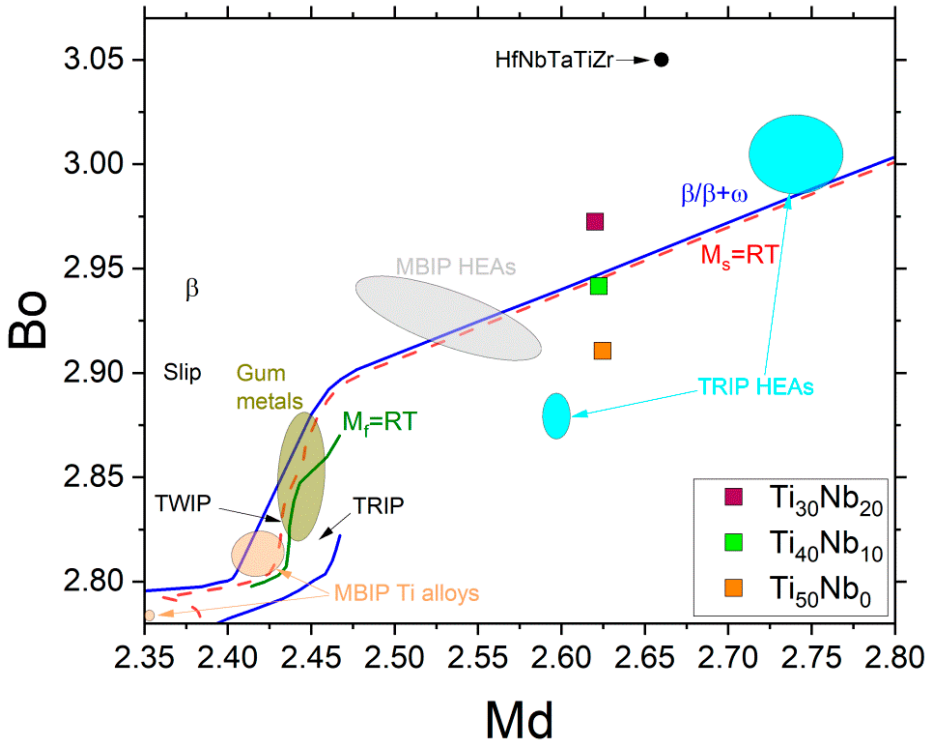


Figure 8. Positions of the program alloys on the Bo–Md map. The references used for plotting this map can be found elsewhere [39].

However, it should be noted that the developed alloys (Ti30Nb20 and Ti40Nb10) have properties that make them highly attractive for biomedical application, owing to a combination of very high yield strengths (1090 and 930 MPa, respectively), low Young's moduli (~78 and ~69, respectively), and reasonable ductility. The results of the cytotoxicity assay also show that the Ti40Nb10 alloy has a somewhat low cytotoxic effect, while Ti50Nb0 can be considered an absolutely biocompatible alloy. However, the Ti30Nb20 alloy has a more pronounced cytotoxic effect (without causing total cell death) that inhibits the proliferation processes and triggers MSC apoptosis.

5. Conclusions

In this study, the structure and mechanical behavior of Ti(50-x)Zr38NbxTa8Sn4 high-entropy alloys with x = 0, 10, and 20 at.% were investigated. The following conclusions were drawn:

The initial microstructure of all the alloys consisted of bcc equiaxed grains. An increase in the Ti/Nb ratio resulted in grain coarsening, from 115 ± 30 μm in the Ti30Nb20 alloy to 250 ± 60 μm and 280 ± 70 μm in the Ti40Nb10 and Ti50Nb0 alloys, respectively.

The Ti30Nb20 and Ti40Nb10 alloys showed significantly higher (>900 MPa) values of yield strength compared to the Ti50Nb0 alloy (<700 MPa). The ductility of all three alloys was similar (δ = 24–29%). However, the Ti30Nb20 and Ti40Nb10 alloys showed a short strain-hardening stage followed by a gradual decrease in flow stress after reaching the yield point. Furthermore, these alloys showed "dropped-then-recovered" strain-hardening rate curves, in contrast to the Ti50Nb0 alloy.

In the Ti30Nb20 and Ti40Nb10 alloys, the formation of dislocation bands and the activation of cross-slip at the microscale, as well as the development of kink bands at the mesoscale, could result in some plastic instability. In contrast, the lamellar-like microstructure with parallel dislocation bands observed in the Ti50Nb0 alloy was associated with a more stable mechanical behavior.

The Ti30Nb20 and Ti40Nb10 alloys developed have properties that make them highly attractive for biomedical application: high yield strengths (1090 and 930 MPa, respectively), low Young's moduli (~78 and ~69 GPa, respectively), reasonable ductility, and excellent biocompatibility.

Author Contributions: Conceptualization, S.Z., N.S. and N.Y.; methodology, M.O., N.Y., V.S. and E.P.; validation, S.Z. and M.O.; formal analysis, S.Z., N.Y. and M.O.; investigation, M.O., N.Y., E.P., E.N., V.S. and S.N.; resources, S.Z.; data curation, S.Z., M.O. and S.N.; writing—original draft preparation, M.O.; writing—review and editing, S.Z., N.S. and N.Y.; visualization, M.O.; supervision, S.Z. and M.O.; project administration, S.Z.; funding acquisition, S.Z. All authors have read and agreed to the published version of the manuscript.

Funding: This research was funded by the Ministry of Science and Higher Education of the Russian Federation, project No. 20180167 "Development of high-entropy alloys for biomedical applications" within the program "Priority-2030". A part of this research (TEM specimens' preparation) was partially funded by the Ministry of Science and Higher Education of the Russian Federation as part of the World-class Research Center program: Advanced Digital Technologies (Contract no. № 075-15-2022-312 dated 20 April 2022).

Institutional Review Board Statement: Not applicable.

Informed Consent Statement: Not applicable.

Data Availability Statement: The raw/processed data required to reproduce these findings cannot be shared at this time as the data also form part of an ongoing study.

Acknowledgments: This work was performed under the framework of the Development Program of Belgorod State University for 2021–2030 ("Priority 2030"). Investigations were carried out using the equipment of the Joint Research Center of Belgorod State National Research University «Technology and Materials» with financial support from the Ministry of Science and Higher Education of the Russian Federation within the framework of agreement No. № 075-15-2021-690 (unique identifier for the project RF—-2296.61321X0030).

Conflicts of Interest: The authors declare no conflict of interest.

References

1. Song, Y.; Xu, D.S.; Yang, R.; Li, D.; Wu, W.T.; Guo, Z.X. Theoretical study of the effects of alloying elements on the strength and modulus of β-type bio-titanium alloys. *Mater. Sci. Eng. A* **1999**, *260*, 269–274. [CrossRef]
2. Long, M.; Rack, H. Titanium alloys in total joint replacement—A materials science perspective. *Biomaterials* **1998**, *19*, 1621–1639. [CrossRef] [PubMed]

3. Braic, V.; Balaceanu, M.; Braic, M.; Vladescu, A.; Panseri, S.; Russo, A. Characterization of multi-principal-element (TiZrNbHfTa)N and (TiZrNbHfTa)C coatings for biomedical applications. *J. Mech. Behav. Biomed. Mater.* **2012**, *10*, 197–205. [CrossRef]
4. Oliveira, J.P.; Panton, B.; Zeng, Z.; Andrei, C.M.; Zhou, Y.; Miranda, R.M.; Fernandes, F.M.B. Laser joining of NiTi to Ti6Al4V using a Niobium interlayer. *Acta Mater.* **2016**, *105*, 9–15. [CrossRef]
5. Miracle, D.B.; Senkov, O.N. A critical review of high entropy alloys and related concepts. *Acta Mater.* **2017**, *122*, 448–511. [CrossRef]
6. Geetha, M.; Singh, A.K.; Asokamani, R.; Gogia, A.K. Ti based biomaterials, the ultimate choice for orthopedic implants—A review. *Prog. Mater. Sci.* **2009**, *54*, 397–425. [CrossRef]
7. Castro, D.; Jaeger, P.; Baptista, A.C.; Oliveira, J.P. An Overview of High-Entropy Alloys as Biomaterials. *Metals* **2021**, *11*, 648. [CrossRef]
8. Motallebzadeh, A.; Peighambardoust, N.S.; Sheikh, S.; Murakami, H.; Guo, S.; Canadinc, D. Microstructural, mechanical and electrochemical characterization of TiZrTaHfNb and Ti1.5ZrTa0.5Hf0.5Nb0.5 refractory high-entropy alloys for biomedical applications. *Intermetallics* **2019**, *113*, 106572. [CrossRef]
9. Ishimoto, T.; Ozasa, R.; Nakano, K.; Weinmann, M.; Schnitter, C.; Stenzel, M.; Matsugaki, A.; Nagase, T.; Matsuzaka, T.; Todai, M.; et al. Development of TiNbTaZrMo bio-high entropy alloy (BioHEA) super-solid solution by selective laser melting, and its improved mechanical property and biocompatibility. *Scr. Mater.* **2021**, *194*, 113658. [CrossRef]
10. Popescu, G.; Ghiban, B.; Popescu, C.A.; Rosu, L.; Truscă, R.; Carcea, I.; Soare, V.; Dumitrescu, D.; Constantin, I.; Olaru, M.T.; et al. New TiZrNbTaFe high entropy alloy used for medical applications. *IOP Conf. Ser. Mater. Sci. Eng.* **2018**, *400*, 022049. [CrossRef]
11. Akmal, M.; Hussain, A.; Afzal, M.; Lee, Y.I.; Ryu, H.J. Systematic study of (MoTa)xNbTiZr medium- and high-entropy alloys for biomedical implants- In vivo biocompatibility examination. *J. Mater. Sci. Technol.* **2021**, *78*, 183–191. [CrossRef]
12. Yuan, Y.; Wu, Y.; Yang, Z.; Liang, X.; Lei, Z.; Huang, H.; Wang, H.; Liu, X.; An, K.; Wu, W.; et al. Formation, structure and properties of biocompatible TiZrHfNbTa high-entropy alloys. *Mater. Res. Lett.* **2019**, *7*, 225–231. [CrossRef]
13. Gurel, S.; Yagci, M.B.; Canadinc, D.; Gerstein, G.; Bal, B.; Maier, H.J. Fracture behavior of novel biomedical Ti-based high entropy alloys under impact loading. *Mater. Sci. Eng. A* **2021**, *803*, 140456. [CrossRef]
14. Yang, W.; Liu, Y.; Pang, S.; Liaw, P.K.; Zhang, T. Bio-corrosion behavior and in vitro biocompatibility of equimolar TiZrHfNbTa high-entropy alloy. *Intermetallics* **2020**, *124*, 106845. [CrossRef]
15. Węglewski, W.; Bochenek, K.; Basista, M.; Schubert, T.; Jehring, U.; Litniewski, J.; Mackiewicz, S. Comparative assessment of Young's modulus measurements of metal–ceramic composites using mechanical and non-destructive tests and micro-CT based computational modeling. *Comput. Mater. Sci.* **2013**, *77*, 19–30. [CrossRef]
16. Edmondson, J.M.; Armstrong, L.S.; Martinez, A.O. A rapid and simple MTT-based spectrophotometric assay for determining drug sensitivity in monolayer cultures. *J. Tissue Cult. Methods* **1988**, *11*, 15–17. [CrossRef]
17. Jiang, Y.; Wang, X.; Jiang, Z.; Chen, M.; Sun, M.; Zhang, X. Phase transition and mechanical performance evolution in TiVZr-Nbx alloys. *J. Alloys Compd.* **2023**, *937*, 168458. [CrossRef]
18. Gutierrez-Urrutia, I.; Raabe, D. Dislocation and twin substructure evolution during strain hardening of an Fe–22wt.% Mn–0.6wt.% C TWIP steel observed by electron channeling contrast imaging. *Acta Mater.* **2011**, *59*, 6449–6462. [CrossRef]
19. Welsch, E.; Ponge, D.; Hafez Haghighat, S.M.; Sandlöbes, S.; Choi, P.; Herbig, M.; Zaefferer, S.; Raabe, D. Strain hardening by dynamic slip band refinement in a high-Mn lightweight steel. *Acta Mater.* **2016**, *116*, 188–199. [CrossRef]
20. Rho, J.Y.; Tsui, T.Y.; Pharr, G.M. Elastic properties of human cortical and trabecular lamellar bone measured by nanoindentation. *Biomaterials* **1997**, *18*, 1325–1330. [CrossRef]
21. Yeh, J.-W. Alloy Design Strategies and Future Trends in High-Entropy Alloys. *JOM.* **2013**, *65*, 1759–1771. [CrossRef]
22. Hu, Q.-M.; Li, S.-J.; Hao, Y.-L.; Yang, R.; Johansson, B.; Vitos, L. Phase stability and elastic modulus of Ti alloys containing Nb, Zr, and/or Sn from first-principles calculations. *Appl. Phys. Lett.* **2008**, *93*, 121902. [CrossRef]
23. Miura, K.; Yamada, N.; Hanada, S.; Jung, T.-K.; Itoi, E. The bone tissue compatibility of a new Ti–Nb–Sn alloy with a low Young's modulus. *Acta Biomater.* **2011**, *7*, 2320–2326. [CrossRef] [PubMed]
24. Hanada, S.; Masahashi, N.; Jung, T.K. Effect of stress-induced α" martensite on Young's modulus of β Ti–33.6Nb–4Sn alloy. *Mater. Sci. Eng. A* **2013**, *588*, 403–410. [CrossRef]
25. Li, P.; Ma, X.; Wang, D.; Zhang, H. Microstructural and Mechanical Properties of β-Type Ti–Nb–Sn Biomedical Alloys with Low Elastic Modulus. *Metals* **2019**, *9*, 712. [CrossRef]
26. Ozaki, T.; Matsumoto, H.; Watanabe, S.; Hanada, S. Beta Ti Alloys with Low Young's Modulus. *Mater. Trans.* **2004**, *45*, 2776–2779. [CrossRef]
27. Fleischer, R.L. Substitutional solution hardening. *Acta Metall.* **1963**, *11*, 203–209. [CrossRef]
28. Juan, C.-C.; Tsai, M.-H.; Tsai, C.-W.; Hsu, W.-L.; Lin, C.-M.; Chen, S.-K.; Lin, S.-J.; Yeh, J.-W. Simultaneously increasing the strength and ductility of a refractory high-entropy alloy via grain refining. *Mater. Lett.* **2016**, *184*, 200–203. [CrossRef]
29. Eleti, R.R.; Stepanov, N.; Zherebtsov, S. Mechanical behavior and thermal activation analysis of HfNbTaTiZr body-centered cubic high-entropy alloy during tensile deformation at 77 K. *Scr. Mater.* **2020**, *188*, 118–123. [CrossRef]
30. Cao, S.; Zhou, X.; Lim, C.V.S.; Boyer, R.R.; Williams, J.C.; Wu, X. A strong and ductile Ti-3Al-8V-6Cr-4Mo-4Zr (Beta-C) alloy achieved by introducing trace carbon addition and cold work. *Scr. Mater.* **2020**, *178*, 124–128. [CrossRef]
31. Yurchenko, N.; Panina, E.; Tojibaev, A.; Novikov, V.; Salishchev, G.; Zherebtsov, S.; Stepanov, N. Effect of B2 ordering on the tensile mechanical properties of refractory AlxNb40Ti40V20−x medium-entropy alloys. *J. Alloys Compd.* **2023**, *937*, 168465. [CrossRef]

32. Wang, S.-P.; Ma, E.; Xu, J. New ternary equi-atomic refractory medium-entropy alloys with tensile ductility: Hafnium versus titanium into NbTa-based solution. *Intermetallics* **2019**, *107*, 15–23. [CrossRef]
33. Kumnorkaew, T.; Lian, J.; Uthaisangsuk, V.; Zhang, J.; Bleck, W. Low carbon bainitic steel processed by ausforming: Heterogeneous microstructure and mechanical properties. *Mater. Charact.* **2022**, *194*, 112466. [CrossRef]
34. Yurchenko, N.; Panina, E.; Tojibaev; Zherebtsov, S.; Stepanov, N. Overcoming the strength-ductility trade-off in refractory medium-entropy alloys via controlled B2 ordering. *Mater. Res. Lett.* **2022**, *10*, 813–823. [CrossRef]
35. Nizolek, T.; Mara, N.A.; Beyerlein, I.J.; Avallone, J.T.; Pollock, T.M. Enhanced Plasticity via Kinking in Cubic Metallic Nanolaminates. *Adv. Eng. Mater.* **2015**, *17*, 781–785. [CrossRef]
36. Weiss, I.; Semiatin, S.L. Thermomechanical processing of beta titanium alloys—An overview. *Mater. Sci. Eng. A* **1998**, *243*, 46–65. [CrossRef]
37. Abdel-Hady, M.; Hinoshita, K.; Morinaga, M. General approach to phase stability and elastic properties of b-type Ti-alloys using electronic parameters. *Scr. Mater.* **2006**, *55*, 477–480. [CrossRef]
38. Lilensten, L.; Couzinie, J.-P.; Bourgon, J.; Perriere, L.; Dirras, G.; Prima, F.; Guillot, I. Design and tensile properties of a bcc Ti-rich high-entropy alloy with transformation-induced plasticity. *Mater. Res. Lett.* **2017**, *5*, 110–116.
39. Zherebtsov, S.; Yurchenko, N.; Panina, E.; Tojibaev, A.; Tikhonovsky, M.; Salishchev, G.; Stepanov, N. Microband-induced plasticity in a Ti-rich high-entropy alloy. *J. Alloys Compd.* **2020**, *842*, 155868. [CrossRef]

Disclaimer/Publisher's Note: The statements, opinions and data contained in all publications are solely those of the individual author(s) and contributor(s) and not of MDPI and/or the editor(s). MDPI and/or the editor(s) disclaim responsibility for any injury to people or property resulting from any ideas, methods, instructions or products referred to in the content.